Surfactant-modifications of Na^+–beidellite for the preparation of TiO_2–Bd supported photocatalysts: II—Physico-chemical characterization and photocatalytic properties

B. Rhouta [a,*], L. Bouna [a], F. Maury [b], F. Senocq [b], M.C. Lafont [b], A. Jada [c], M. Amjoud [a], L. Daoudi [d]

[a] Laboratoire de Matière Condensée et Nanostructures (LMCN), Faculté des Sciences et Techniques Guéliz, Université Cadi Ayyad, BP 549, Marrakech, Morocco
[b] CIRIMAT, Université de Toulouse, CNRS-UPS-INP, ENSIACET, 4 allée Emile Monso, BP 44362, 31030Toulouse cedex 4, France
[c] Institut de Sciences des Matériaux de Mulhouse (IS2M), LRC 7228—CNRS, 15 rue Jean Starcky, BP 2488, 68057Mulhouse cedex, France
[d] Laboratoire de Géosciences et Géoenvironnement, Faculté des Sciences et Techniques Guéliz, Université Cadi Ayyad, BP 549, Marrakech, Morocco

Keywords:
Beidellite
TiO_2
Photocatalysis
Surfactant
Cethyltrimethylammonium bromide (CTAB)
Nanocomposites

A B S T R A C T

This work deals with the study of the effect of the amount of cethyltrimethylammonium bromide (CTAB) surfactant, used in the preparation of starting organobeidellites, on physico-chemical properties and photocatalytic activity of TiO_2 supported beidellite (Bd) nanocomposites against the removal of Orange G (OG) dye from aqueous media. A structural study of organobeidellites used as starting materials was reported in a companion paper. Here, physico-chemical characterizations of the nanocomposite photocatalysts show that TiO_2 supported on Bd beforehand organomodified with an amount of CTAB equivalent to 3 CEC of smectite ($3CTA^+$–Bd) exhibits thin fine grained (≈10 nm) features which remarkably remained stable in the form of photoactive anatase up to 750 °C. Comparatively, the TiO_2 coating grown on Bd previously rendered organophilic by using an amount of CTAB equivalent to 5 CEC of Clay mineral ($5CTA^+$–Bd) appears thicker and more porous with larger nanoparticles (≈25 nm) which is prone to be readily converted into less photoactive rutile as observed near 700 °C. This is likely due to its development mainly outside Bd interlayer spaces promoted by outer organophilic environment created by the adsorption of CTA^+ excess. In both cases, anatase is still present as minor phase up to 900 °C. As a result of these differences a significant improvement of the photocatalytic activity of TiO_2 supported Bd nanocomposite prepared starting from $3CTA^+$–Bd is observed compared to that from $5CTA^+$–Bd. For instance, the total elimination of the pollutant from the aqueous solution occurs within about 45 min when using the $3CTA^+$–Bd–TiO_2 photocatalyst instead of 90 min using the $5CTA^+$–Bd–TiO_2 sample. Furthermore, the best TiO_2–Bd supported photocatalyst is also found more efficient than a pure TiO_2 xerogel sample.

1. Introduction

Owing to its ability to provide strong oxidant species (holes h^+ and radicals $^{\cdot}OH$) upon UV irradiation of semiconductor oxides, heterogeneous photocatalysis emerges as an efficient alternative technique able to decompose and to mineralize bio-recalcitrant organic pollutants in the form of CO_2 and H_2O (Robertson, 1996; Herrmann, 1999; Fujishima et al., 2000; Carp et al., 2004; Fujishima and Zhang, 2006; Paz, 2006). In this respect, commercial TiO_2 nanopowder as Degussa P25, made up of anatase (80%) and rutile (20%), is considered as the most active photocatalyst used in wastewater treatment (Herrmann, 1999; Nieto-Suárez et al., 2009). Nevertheless, TiO_2 powder nanoparticles easily agglomerate which reduces photonic efficiency for most degradation processes to less than 10% (Houari et al., 2005). Furthermore, due to their micrometric sizes, their use requires, for being recovered from water decontaminated by TiO_2 slurry, to implement costly microfiltration processes (Herrmann, 1999; Carp et al., 2004; Houari et al., 2005; Liu et al., 2009). Therefore, researches recently have focused on improving photocatalytic activity via the development of TiO_2 supported photocatalysts.

Clay minerals are considered as promising supports due to their interesting inherent properties, namely their adsorption capacity, high surface area, multi-scale porosity and their ability to be bounded to chemical compounds (An et al., 2008; Aranda et al., 2008; Rhouta et al., 2008; Liu et al., 2009; Nieto-Suárez et al., 2009). In this respect, the immobilization of TiO_2 anatase nanoparticles (average size 10 nm) onto stevensite particles by solvothermal method was recently reported (Bouna et al., 2014) and onto fiber surfaces of palygorskite via a colloidal sol–gel route (Bouna et al., 2011). In this last route in particular, TiO_2 immobilization was promoted after the clay minerals were rendered organophilic by adsorption and/or intercalation of an amount of CTAB surfactant equivalent to 3 CEC of clay mineral. This amount of CTAB was not varied around the 3CEC value. Thus, there is no systematic

* Corresponding author.
E-mail address: b.rhouta@uca.ma (B. Rhouta).

study depending on the clay material undertaken to establish the optimal amount of the surfactant yielding to an efficient supported photocatalyst, in terms of size and distribution of deposited TiO_2 nanoparticles and consequently of photocatalytic efficiency.

In a first part of this work, the effect of surfactant modifications of Na^+–Bd on the structure of these organobeillites has been investigated. In this second part, the effects of CTAB loadings on Bd on the microstructure of supported TiO_2 and afterwards on the photocatalytic activity of this TiO_2–Bd nanocomposite are investigated.

2. Experimental

2.1. Materials

Titanium isopropoxide (TTIP), isopropanol and anionic dye orange G (OG) chemicals were purchased from Aldrich and used without further purification. For comparing the effect of surfactant loads on the main features and properties of TiO_2 supported Bd nanocomposites, two organomodified Bd were considered. They were obtained, as described in part I, with an amount of CTAB surfactant equivalent to 3 CEC (namely $3CTA^+$–Bd) and 5 CEC ($3CTA^+$–Bd).

2.2. Preparation of TiO_2 supported beidellite nanocomposites

An amount of 5 cm^3 of TTIP was added to a dispersion of 1 g of either $3CTA^+$–Bd or $5CTA^+$–Bd in isopropanol (7 cm^3). Afterwards, water was added drop wise under stirring until the spontaneous formation of a gel. The corresponding gels, labeled $3CTA^+$–Bd–Ti and $5CTA^+$–Bd–Ti respectively, were dried at 60 °C for 2 days and thereafter, as further justified, air annealed at 600 °C for 1 h to promote the formation of TiO_2. The samples hence obtained were accordingly designated as $3CTA^+$–Bd–TiO_2 and $5CTA^+$–Bd–TiO_2 respectively.

In parallel, TiO_2 xerogel was prepared according to the above conditions, i.e. hydrolyzing a mixture of 5 cm^3 of TTIP and isopropanol ($\approx$40% *v/v*) by slow addition of increasing amounts of water. The TiO_2 xerogel sample was dried at 60 °C for 2 days and heated in air at 600 °C for 1 h to give TiO_2 powder (designated as pure TiO_2).

2.3. Characterizations

The structural changes of TiO_2 upon heating different gel samples, as prepared in the presence or not of either unmodified Bd or organomodified Bd, were analyzed in situ versus the temperature by X-ray diffraction (XRD) through the two-theta range 2–60 deg using a Bruker D8 Advance diffractometer equipped with a Vantec Super Speed detector and a MRI radiation heating chamber (Bragg–Brentano configuration; Ni filtered Cu K_α radiation). The diffractograms were recorded every 50 °C from the room temperature to 950 °C. An isotherm was maintained at each level for 40 min to record the pattern then the temperature was increased using a ramp of 1 deg s^{-1}. XRD at room temperature was recorded on pure TiO_2 and TiO_2–Bd samples, prepared after air annealing of corresponding gels at 600 °C for 1 h, in the same angular range using a Seifert XRD 3000TT diffractometer equipped with a graphite monochromator (Bragg–Brentano configuration; Cu K_α radiation).

A JEOL JEM 2010 transmission electron microscopy (TEM) equipped with a TRACOR EDS analyzer was used for characterizing clay particles and performing local elemental composition. Fourier transformed infrared (FTIR) spectroscopic studies were undertaken using a Nicolet 5700 spectrometer under ambient conditions in the frequency range of 400–4000 cm^{-1} using KBr pellets. The pellets contained a mixture of 2 mg of clay material with 198 mg of KBr ($\approx$1 wt.%). The specific surface areas were determined by the Brunauer–Emmett–Teller (BET) method from nitrogen adsorption isotherms at 77 K using an adsorption analyzer from Micromeritics (ASAP 2020 V 3.01 H). In order to investigate the effect of TiO_2 deposited on Bd on the electrical properties of the clay aqueous dispersions, the Points of Zero Charge (PZC) of the various samples were evaluated by titration of the aqueous dispersion of starting Na^+-exchanged Bd (Na^+–Bd), pure TiO_2 and the two TiO_2–Bd nanocomposites ($3CTA^+$–Bd–TiO_2 and $5CTA^+$–Bd–TiO_2), with a cationic surfactant (cetyltrimethylammonium chloride, CTAC). For this purpose, the streaming induced potential (SIP) of various samples was measured by using an electrical potential device (Particle Charge Detection, PCD, Müteck instrument), as described elsewhere (Jada et al., 2006; Bouna et al., 2010).

TiO_2 amounts contained in both the supported photocatalysts were determined by Induction Coupled Plasma (ICP) by mean of a unit of Thermo Electron Series X2 equipped with a Meinhard nebulizer and a detector type SimulScan FTE.

2.4. Photocatalytic activity

The photocatalytic activity of different samples was evaluated at pH around 6 by measuring the decomposition rate of the model pollutant OG (Orange G) in aqueous solutions containing the supported photocatalyst according to a procedure previously reported (Sarantopoulos et al., 2009) and adapted to the dispersion of supported powder photocatalysts in further papers (Rhouta et al., 2008; Bouna et al., 2013; Bouna et al., 2014). The degradation reaction was performed in a batch quartz reactor (40 × 20 × 36 mm^3) placed in a thermostated chamber (25 °C) under the UV light of a lamp (HPLN Philips 125 W) emitting at 365 nm. The reactor was irradiated with a photon flux of about 1 mW cm^{-2} by adjusting the distance to the lamp so that it simulates the UV intensity of solar spectrum on the earth (Hofstadler et al., 1994). This lamp was chosen because the OG absorption is negligible at this wavelength and, as a result, the direct photolysis of the solution (i.e. without photocatalyst) was found negligible for more than 24 h. The photocatalyst powder of either TiO_2–Bd nanocomposites or pure TiO_2 powders prepared from TTIP was added to 25 cm^3 of OG solution (10^{-5} M) in an amount equal to 0.8 g dm^{-3}. This catalyst mass was found as optimum to avoid excess of catalyst and to ensure an efficient absorption of the photons (Bouna et al., 2013). The dispersion was agitated with an inert Teflon magnetic stirrer. To determine the dye concentration, aliquots were taken from the mixture at regular time intervals and centrifuged at 12,500 rpm for 5 min. The OG concentration in the supernatant was determined by measuring the absorbance at 480 nm using a UV–VIS-NIR spectrophotometer (Perking Elmer lambda 19).

3. Results and discussion

3.1. Phase identification

Fig. 1a and b represents in situ XRD patterns versus annealing temperature in air of gels leading to the samples $3CTA^+$–Bd–Ti and $5CTA^+$–Bd–Ti, respectively. In both cases, TiO_2 begins to crystallize beyond 400 °C in the form of anatase (A) (JCPDS file 99-201-5379) as evidenced for instance by the (101) and (200) reflections at *ca.* 25 and 48°, respectively. Ambient XRD pattern of as-prepared $3CTA^+$–Bd–Ti sample, i.e. including a thermal treatment at 600 °C in air has further confirmed the crystallization of TiO_2 anatase as single phase upon annealing at this temperature (Fig. 2). This is evidenced by the appearance of exclusively its characteristic reflections at 25, 38, 48, 54 and 55°. Furthermore, this pattern neatly revealed that the Bd remains stable at 600 °C as evidenced by the characteristic (001) basal reflection at 8.7° along with reflections at 20 and 26.7° pertaining to remaining quartz impurities (Fig. 2). The (001) basal reflection of the Bd appears attenuated as a result likely of the screening due to the coverage of its particles with the anatase coating.

It is worth noting that anatase begins to transform into rutile starting from 700 °C in the sample $5CTA^+$–Bd—Ti (Fig. 1b) and relatively lately at 750 °C for the specimen $3CTA^+$–Bd–Ti (Fig. 1a) as evidenced by the

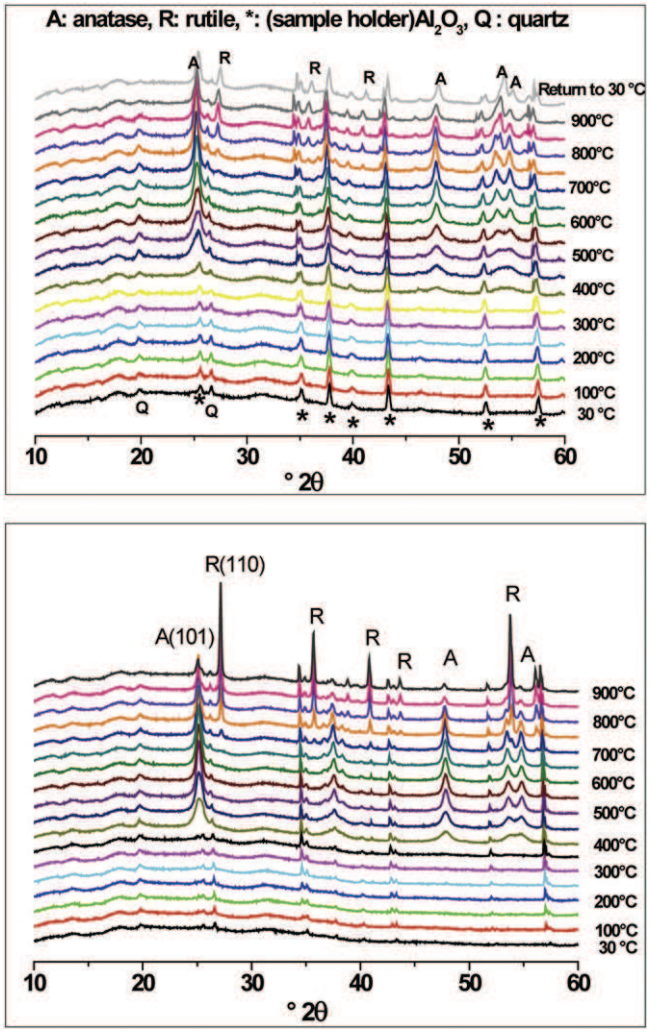

Fig. 1. In-situ XRD patterns versus annealing temperature in air of TiO_2–Bd nanocomposites prepared starting from organobeidellites $3CTA^+$–Bd (a) and $5CTA^+$–Bd (b). The stackings show differences in the crystallinity of anatase (A) and its transformation into rutile (R) by increasing the temperature (Q: quartz; * alumina from the sample holder).

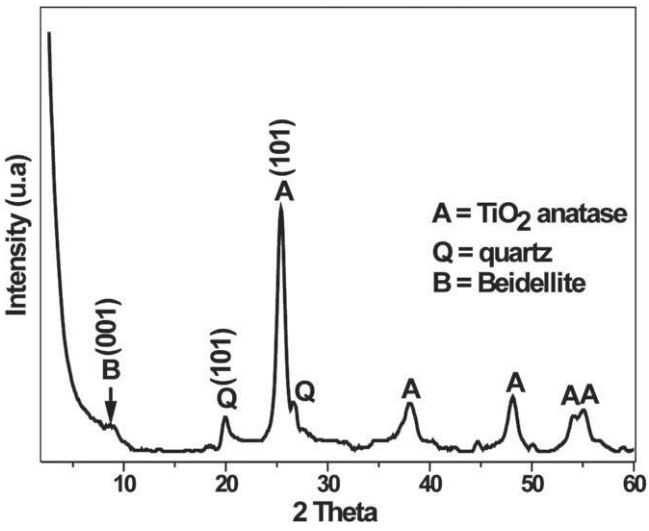

Fig. 2. XRD pattern recorded on TiO_2–Bd nanocomposite prepared upon annealing in air at 600 °C for 1 h and starting from Bd organomodified as precursor with an amount of CTAB surfactant equivalent to 3 CEC of clay mineral. The (001) basal reflection of Bd clearly appears near 9°.

emergence of characteristic peaks (R) at 27.1, 35.7, 40.8, 43.6 and 53.7°. As the annealing temperature increases, the intensities of rutile reflections increase at the expense of those of anatase more rapidly in the case of the sample $5CTA^+$–Bd–Ti in comparison with $3CTA^+$–Bd–Ti. Although TiO_2 anatase reflections are always observed in the XRD pattern recorded at 900 °C in both samples, hence traducing a good thermal stability of this TiO_2 photoactive phase, the occurrence of anatase transformation into rutile is much more pronounced in the sample $5CTA^+$–Bd–Ti with respect to $3CTA^+$–Bd–Ti as revealed by the intensity ratio of the main peaks of both phases at 900 °C. This result denoted that the stabilization of anatase is much favored in the presence of the Bd beforehand organomodified with an amount of CTAB surfactant equivalent to 3 CEC rather than 5 CEC.

Unlike as-prepared titania functionalized CTA modified Bd samples ($3CTA^+$–Bd–Ti and $5CTA^+$–Bd–Ti) that did not exhibit crystalline TiO_2 phase before calcinations at 400 °C (Fig. 1a and b), in situ XRD patterns versus the temperature of titania xerogel (TiO_2 xerogel) reveal the presence of nanocrystalline anatase with broad peaks at 25.2, 37.5, 47.9 and 54.4° at room temperature (Fig. 3), i.e. before any calcination. As the temperature increases, the crystallinity of anatase is improved as supported by the higher intensity and lower full width at half maximum (FWHM) of the XRD peaks. It is worth noting that the anatase/rutile transition occurs in pure TiO_2 at relatively lower temperature (≈600 °C) with respect to TiO_2 formed on organomodified Bd ($3CTA^+$–Bd–TiO_2, $5CTA^+$–Bd–TiO_2) and the total transformation into rutile was effective beyond 650 °C. This result demonstrates the beneficial effect of organobeideillite to stabilize the photoactive TiO_2 anatase phase especially that prepared with an amount of CTAB surfactant equivalent to 3 CEC.

3.2. TiO_2 crystallite size variation versus annealing temperature

Fig. 4 depicts the variations of crystallites sizes determined from the FWHM of (101) anatase and (110) rutile XRD reflections according to Scherrer's law versus annealing temperature of pure TiO_2 and TiO_2 developed in the presence of the organomodified Bd $3CTA^+$–Bd and $5CTA^+$–Bd. For pure TiO_2, the average crystallite size of anatase continuously increases from 5 nm for as-prepared TiO_2 xerogel sample to 30 nm after annealing at 650 °C. Beyond this temperature, the rutile phase emerges with a crystallite size of *ca.*40 nm which rapidly grows with the annealing temperature to reach 130 nm at 900 °C while anatase is negligible above 700 °C. In contrast, in the case of TiO_2 supported on Bd beforehand organomodified with amounts of CTAB surfactant

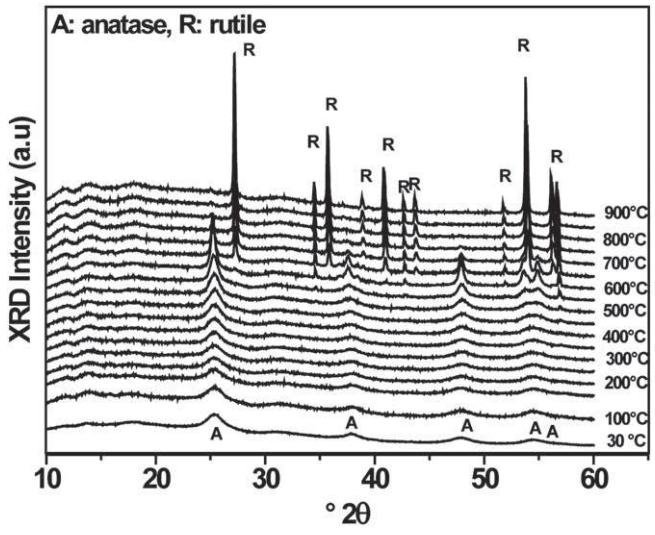

Fig. 3. In situ XRD of a TiO_2 xerogel sample as a function of the annealing temperature in air showing that the transformation of anatase (A) to rutile (R) occurs at *ca.*600 °C.

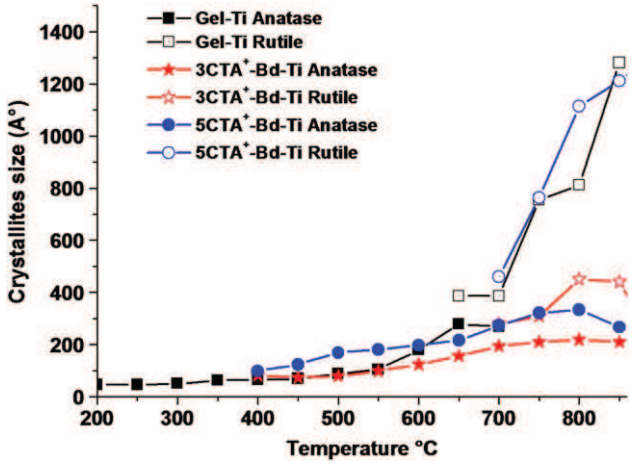

Fig. 4. Variation of the average crystallite size of anatase (filled) and rutile (empty) for a pure TiO_2 sample (square), $3CTA^+$–Bd–TiO_2 (star) and $5CTA^+$–Bd–TiO_2 (circles) as a function of annealing temperature. Crystallite sizes were determined from (101) and (110) of anatase and rutile, respectively.

equivalent to 3 and 5 CEC, crystalline anatase begins to be detected around 400 °C with an average crystallites size of about 9 nm. Beyond this temperature, the crystallite size of anatase immobilized on the Bd organomodified with 5 CEC of CTAB continuously increases in a relatively faster way with respect to that developed on the Bd organomodified with 3 CEC of CTAB to reach approximately 33 nm at about 800 °C. In the presence of the Bd modified with 3 CEC of CTAB, it is noteworthy that the average crystallite size of anatase remains almost constant for temperature ranging from 400 to 550 °C at 9–10 nm and slightly increases to reach a plateau in the temperature range of 700–900 °C at *ca.*20 nm. Likewise, rutile formed beyond 700 °C in contact with 5CEC–Bd exhibits almost similar variation of the crystallite size than that described above for pure TiO_2 whereas rutile formed in the presence of 3CEC–Bd presents significantly smaller changes with crystallite sizes ranging from 30 to 40 nm in temperature range of 750–900 °C. Interestingly, these results seem to demonstrate that organophilic surfaces, mainly interlayer regions, offered by the Bd modified with an amount equivalent to 3 CEC of CTAB prevent the excessive growth of TiO_2 nanoparticles, especially those of anatase, and thus delay its conversion into the less photoactive rutile phase.

3.3. Functional groups analysis

Fig. 5 gathers FTIR spectra recorded on starting clay mineral (Na^+–Bd), pure TiO_2 and TiO_2 functionalized organobeidellites ($3CTA^+$–Bd–TiO_2 and $5CTA^+$–Bd–TiO_2) formed upon air annealing at 600 °C for 1 h. The stretching vibrations at 2924 and 2853 cm^{-1} as well as their corresponding deformations at 1490 and 1470 cm^{-1}, which are fingerprints of CTAB surfactant species, are no longer observed in both TiO_2 functionalized Bd. This supports the quite complete removal of surfactant entities upon annealing at 600 °C and states their unique role in promoting the assembling of the Ti alkoxide precursor for generating the TiO_2 network (Aranda et al., 2008). Furthermore, the spectra of the two TiO_2 functionalized Bd somewhat exhibit, over most vibrations zones, bands shapes similar to that of TiO_2 synthesized in the absence of organobeidellite. The large complex band extending over frequency range of 400–800 cm^{-1} could be due to vibrations of Ti—O and Ti—O—Ti bonds in the TiO_2 structure (Bezrodna et al., 2003; Tong et al., 2008). Nevertheless, the bands at 3700 and 692 cm^{-1}, corresponding to kaolinite impurity (Bouna et al., 2012), as well as peaks at 3622 and 912 cm^{-1}, ascribed to stretching (ν) and deformation (δ) vibrations of hydroxyls in the [Al_2-OH] configuration respectively (Bouna et al., 2012), are observed in starting Bd (Na^+–Bd) but are not clearly resolved in both TiO_2–Bd nanocomposites ($3CTA^+$–Bd–TiO_2 and $5CTA^+$–Bd–TiO_2). Likewise, amongst the intense and sharp bands at 420, 470 and 530 cm^{-1}, corresponding to SiO deformation vibrations in clay mineral, only the band at 470 cm^{-1} is clearly visible. Also, the band at 1034 cm^{-1}, corresponding to stretching vibration of Si—O constituting the skeleton of Bd (Bouna et al., 2012) which was not obviously detected in pure TiO_2 spectrum, appears more intense and resolved in the two TiO_2 functionalized Bd. These FTIR results indicate that some characteristic vibration bands of Bd are likely weakened by the TiO_2 conformal coating or overlaid with bands of the oxide in agreement with XRD results.

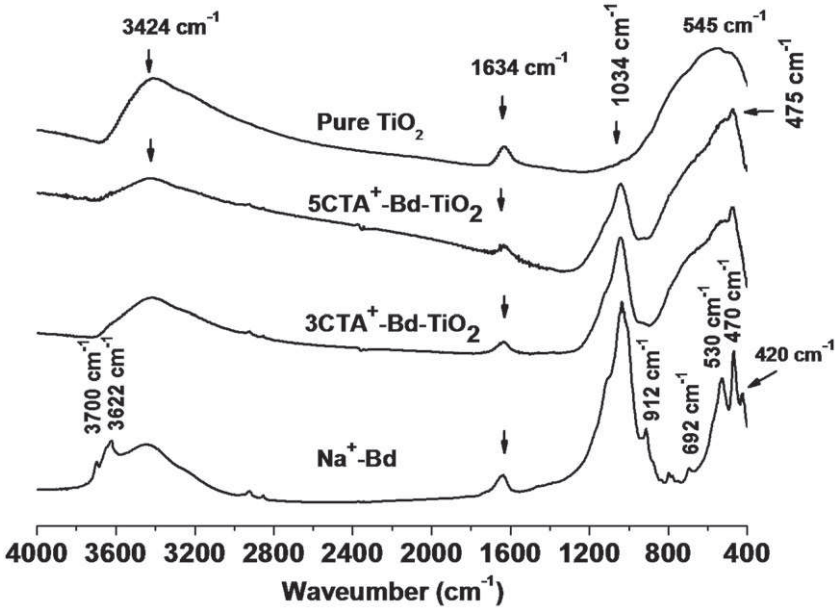

Fig. 5. FTIR spectra recorded on starting Bd (Na^+–Bd), pure TiO_2 and TiO_2 supported Bd ($3CTA^+$–Bd–TiO_2 and $5CTA^+$–Bd–TiO_2) developed upon air annealing at 600 °C for 1 h starting from organobeidellites ($3CTA^+$–Bd and $5CTA^+$–Bd, respectively).

3.4. Microstructural characterizations

XRD and FTIR results were further supported by TEM observations. Indeed, with respect to micrographs of starting Bd (Na^+–Bd) (Fig. 6a and b), the TEM analysis of samples 3CTA^+–Bd–TiO_2(Fig. 6c) and 5CTA^+–Bd–TiO_2(Fig. 6d) showed clearly the deposition of anatase onto the Bd particles. This was confirmed by EDS and by selected area microdiffraction (data not reported). Nevertheless, the microstructure of anatase coatings appeared different depending on the amount of CTAB used in the organomodification process. In fact, the anatase coating grown on Bd particles beforehand modified with an amount of CTAB equivalent to 5 CEC appears thicker and highly porous due to the agglomeration of TiO_2 nanoparticles whose average size is about 25 nm (Fig. 6d). This coating appears to develop essentially on external surfaces of Bd particles by likely forming a matrix trapping Bd layers packets inside it. In contrast, the anatase coating directly grown on Bd previously modified by an amount of CTAB equivalent to 3 CECis thinner and it exhibits a homogeneous distribution of very fine and monodisperse anatase nanoparticles with a lower average size of about 12 nm (Fig. 6c). In this case, anatase nanoparticles appear to be supported on surfaces of more or less delaminated Bd layers.

These differences could be ascribed to the difference in the amount of adsorbed organocation excesses at external surfaces of the clay mineral particles in both the samples. Indeed, as evidenced from CHN and TG analyses in the companion paper of part I, although beidellite interlayer spaces are much expanded by the arrangement of CTA^+ species there in the form of bilayer paraffin upon Bd organomodification with amount equivalent to 5 fold CEC, they likely could not be fully acceded by titanium isopropoxide precursor entities. This access might be hindered by the adsorption of the important excess of CTA^+ entities outside interlayer regions of the clay mineral which create organophilic environment suitable to the assembling of Ti alkoxide and afterwards to the development of outer TiO_2 network. In contrast, the amount of CTA^+ on Bd particles external surfaces in 3CTA^+–Bd organobeidellite is relatively lower that Ti alkoxide could penetrate Bd interlayer regions, rendered organophilic due the disposition of CTA^+ entities in the form of monolayer paraffin, where they could get hydrolyzed and condensed to promote Bd delamination and the organization of the formed nanoparticles of TiO_2(Letaïef et al., 2006; Manova et al., 2010; Ruiz-Hitzky and Aranda, 2014).

3.5. Electrokinetic behavior

The conformal coating of Bd particles by a TiO_2 thin films was further confirmed by monitoring the variation of the streaming induced potential (SIP) upon titration of dispersions of pure TiO_2, starting Bd, 3CTA^+–Bd–TiO_2 and 5CTA^+–Bd–TiO_2 with CTAC surfactant. Indeed, Fig. 7 reveals that the starting negative surface charge of the Bd is compensated progressively with increasing the amount of CTAC added to clay aqueous dispersion to reach a plateau extending from 5×10^{-3} to 9×10^{-3} mmol beyond which the increase of SIP starts again until the neutral value at 11×10^{-3} mmol corresponding to Point of Zero Charge (PZC). Afterward it stabilizes at positive values. The occurrence of an intermediate plateau can be explained by a transition in surfactant species arrangement inside Bd interlayer spaces from monolayer to bilayer configuration as evidenced by XRD in the companion paper. The reversal of SIP sign beyond PZC is due to CTAC excess likely adsorbed on external surfaces of the clay mineral particles in agreement with CHN and TG analyses of part I. On the other hand, pure TiO_2 particles were initially negatively charged, but with lower surface charge

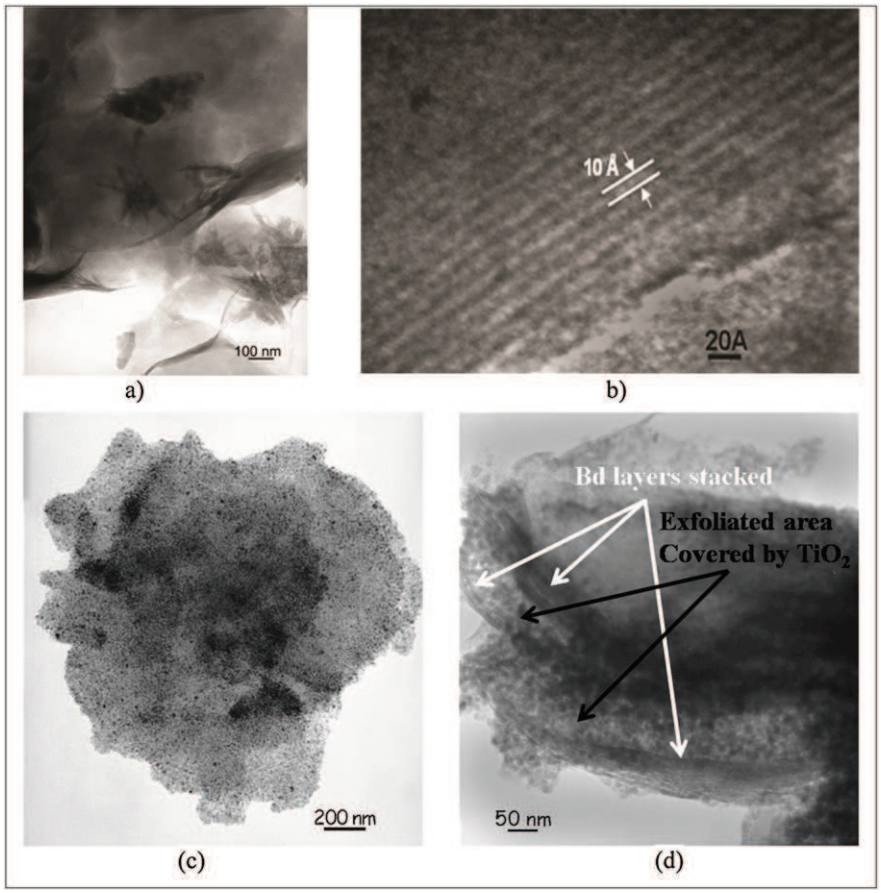

Fig. 6. TEM micrographs of Na^+–Bd showing (a) the petalloïd microstructure and (b) the 10 Å interlayer spaces characteristic of Bd. TEM of the nanocomposites (c) 3CTA^+–Bd–TiO_2 and (d) 5CTA^+–Bd–TiO_2 exhibiting respectively nanometric fine and coarse microstructures of TiO_2 immobilized on Bd surface.

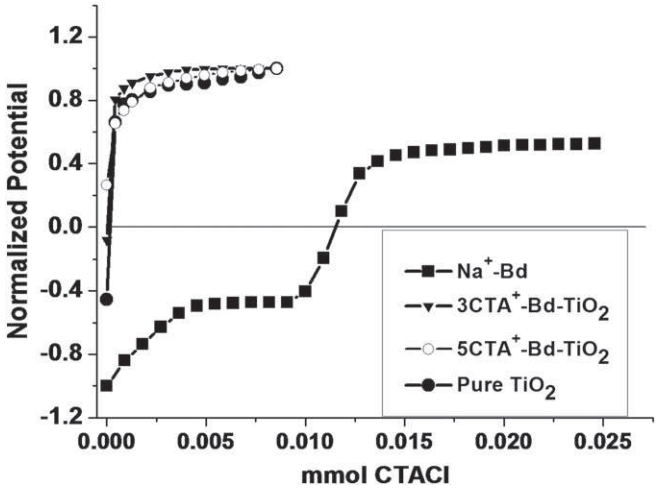

Fig. 7. Variation of the streaming induced potential with CTAC concentration for Na^+–Bd, pure TiO_2, $3CTA^+$–Bd–TiO_2 and $5CTA^+$–Bd–TiO_2.

magnitude in comparison with the starting Bd, as evidenced by the detection of lower negative value of SIP. Furthermore, as can be seen in Fig 7, the addition of CTAC to pure TiO_2 aqueous dispersion leads to electrical surface charge reversal occurring at PZC value significantly lower than that observed for the non-modified Bd. Such difference in the electrokinetic behavior, between pure TiO_2 and Bd, results from the difference in the negative surface charge densities of the samples. At natural pH of the aqueous phase, the Bd particles have higher negative surface charge density as compared to pure TiO_2.

As far as both the TiO_2 functionalized Bd ($3CTA^+$–Bd–TiO_2 and $5CTA^+$–Bd–TiO_2) are concerned, SIP is initially slightly negative as observed for pure TiO_2, which likely denotes the presence of TiO_2 particles on Bd surface, but probably also of some uncoated Bd particles, and rapidly reverses into positive values at relatively much lower PZC around 0.1×10^{-3} mmol of CTAC for afterwards behaving like pure TiO_2. These results confirm that permanent negative charges of Bd particles are screened as a result of their coverage by TiO_2 nanoparticles.

3.6. Textural characterizations

N_2 adsorption–desorption isotherms recorded on Na^+–Bd, pure TiO_2 and TiO_2 functionalized Bd exhibit a shape of type IV according to the IUPAC classification which is a characteristic of porous adsorbents, with pore sizes in the range of 1.5–100 nm (Fig. 8). Specific surface areas determined from these isotherms in the relative pressure range of 0.05–0.33 are about 91 and 82 m^2/g for both TiO_2 supported Bd prepared starting from $3CTA^+$–Bd and $5CTA^+$–Bd, respectively. With respect to Bd whose specific surface area was assessed to be around 82 m^2/g (Bouna et al., 2012), a slight increase in the specific surface area is noted, especially for $3CTA^+$–Bd–TiO_2 whereas that of $5CTA^+$–Bd–TiO_2 remains at the same magnitude order. These results are in concordance with that reported by Manova et al. (2010) for TiO_2–Gafsa smectite nanocomposite. But, they are different from those of Chen et al. (2012) who reported a huge increase by a factor of 20 times of specific surface area of TiO_2-Mt with respect to starting Mt that the authors accounted for a quite complete delaminated structure of the clay mineral. Nevertheless, specific surface areas of both TiO_2–Bd nanocomposites are found higher than that of pure TiO_2 ($\approx$68 cm^2/g). In both the situations, it is worth noting that the beidellite acts a benefic role in increasing surface area of nanocomposite with respect to pure TiO_2 by being dispersed in the TiO_2 matrix in the forms of likely predominantly exfoliated layers for $3CTA^+$–Bd or layers packets for $5CTA^+$–Bd as beforehand evidenced by TEM observations. On the other hand, it should be noted that the observed hysteresis loops differ depending on the nature of the sample. Indeed, the hysteresis loop observed for the starting clay mineral (Na^+–Bd) is of type H_4, revealing a narrow pore-size distribution (Bouna et al., 2012), whereas that occurring for pure TiO_2 is of type H_2, denoting the presence of interconnected mesopores. The hysteresis exhibited by the isotherms of both TiO_2 based Bd nanocomposites are a mixture of H_2/H_4 in which the contribution of H_4 component, observed beyond relative pressures P/P_0 of about 0.85, seems more pronounced in $3CTA^+$–Bd–TiO_2. Concomitantly, the contribution of the H_2 component corresponding to TiO_2 appears predominating in $5CTA^+$–Bd–TiO_2. These results were further supported by depicting pores distribution of all samples investigated herein (Fig. 9). In fact, mesopores in starting Bd are narrow with an average diameter of about 4 nm whereas those of pure TiO_2 are larger around 7 nm in diameter. The pores distribution curves in TiO_2 functionalized

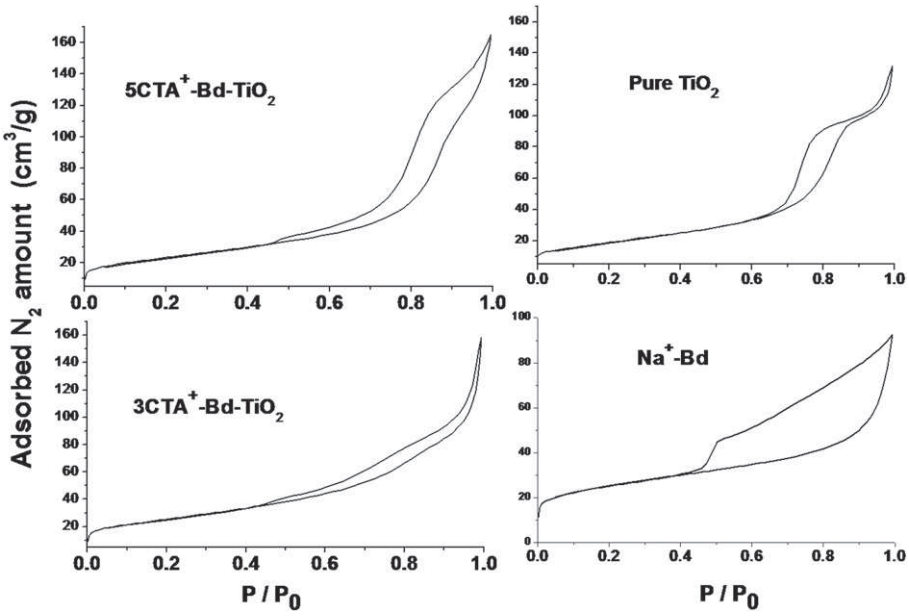

Fig. 8. N_2 Adsorption–desorption isotherms of Na^+–Bd, pure TiO_2, $3CTA^+$–Bd–TiO_2 and $5CTA^+$–Bd–TiO_2 samples.

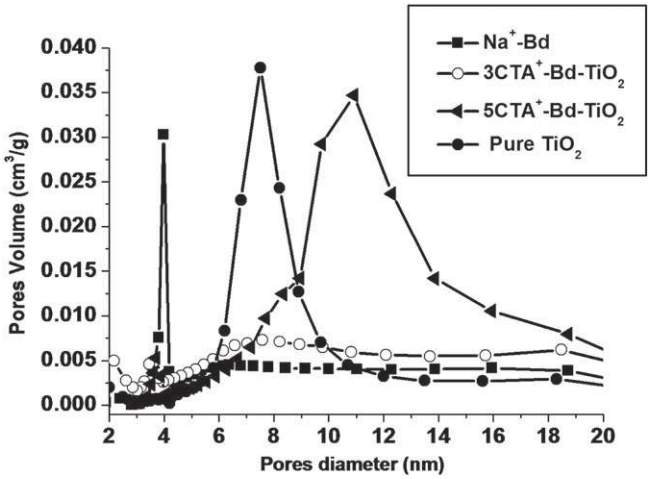

Fig. 9. Porosity distribution of Na^+–Bd, pure TiO_2, $3CTA^+$–Bd–TiO_2 and $5CTA^+$–Bd–TiO_2.

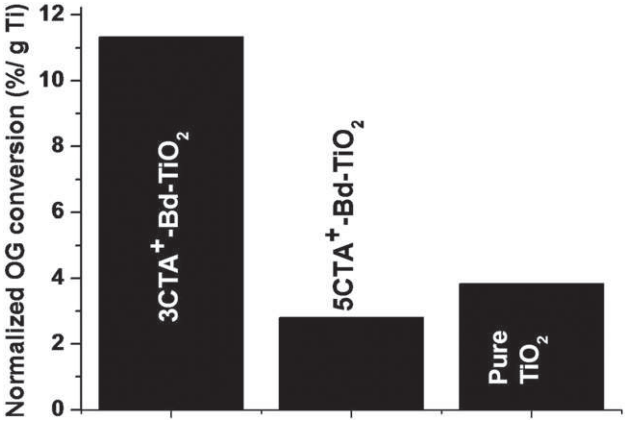

Fig. 11. Orange G proportion normalized by mass of titanium converted by photocatalysis using different catalysts in 15 min.

Bd presents two peaks. The first one is best resolved in both samples and centered at an average pore diameter quite similar to that of Bd. However, while the second one appears broad, diffuse and centered at the same pore diameter of pure TiO_2, it is more intense, better resolved and centered at relatively higher average pore diameter of about 11 nm. These results indicate that organomodification of Bd with an amount of CTAB equivalent to 3 CEC likely results in a supported thin and less porous TiO_2 layer whereas that formed in the presence of Bd organomodified with an amount of CTAB equivalent to 5 CEC is probably thicker and more porous in agreement with TEM observations (Fig. 6c and d). These microstructural differences could be due to the fact that the dispersion of beidellite as exfoliated layers within TiO_2 matrix likely allows to more compact and less porous material which seems to be more predominating in $3CTA^+$–Bd–TiO_2 nanocomposites. Nevertheless, the dispersion of beidellite layers packets in the TiO_2 matrix, promoted by organophilic environment due to the adsorption of important excess of surfactant entities on external surfaces of clay mineral particles, probably yielded to a porous material which is likely more pronounced in $5CTA^+$–Bd–TiO_2 nanocomposite in concordance with TEM observations.

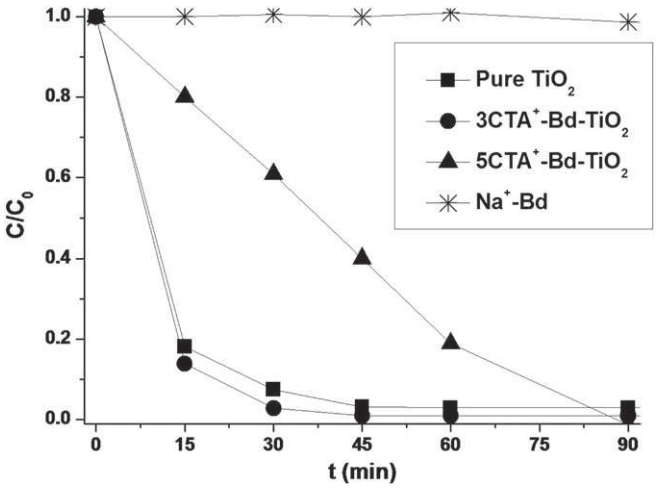

Fig. 10. Change in OG concentration (where C_0 and C are the OG concentrations, respectively, at the initial time t = 0, and after an elapsed time t of the photocatalytic reaction) vs. UV irradiation time of Na^+–Bd, pure TiO_2, $3CTA^+$–Bd–TiO_2 and $5CTA^+$–Bd–TiO_2 samples.

3.7. Photocatalytic activity

The photocatalytic decomposition kinetics of starting Bd, pure TiO_2 and the set of TiO_2 supported Bd synthesized starting from all the organobeidellites differing in CTAB loads were tested against the degradation of OG in aqueous solution. Fig. 10 represents results obtained only on Na^+–Bd and pure TiO_2 along with the two TiO_2 supported Bd ($3CTA^+$–Bd–TiO_2 and $5CTA^+$–Bd–TiO_2). Photocatalytic behavior curves of all supported catalysts developed herein is given in supplementary data (see Fig. 1S). The pristine Bd (Na^+–Bd) does not show photocatalytic activity since no decrease of the OG concentration is observed. In contrast, both TiO_2 functionalized Bd exhibit significant photoactivity as evidenced by the reduction of OG concentration as the UV irradiation time increases. TiO_2 supported on Bd beforehand organomodified with an amount of CTAB equivalent to 3 CEC exhibits slightly higher photocatalytic activity compared to that of pure TiO_2 and it is also much more efficient than that of TiO_2 immobilized on Bd previously rendered organophilic with an amount of the surfactant equivalent to 5 CEC. This is evidenced on one hand by the strong decrease of OG concentration for instance in the first 15 min, revealing a high initial degradation rate of the pollutant, and on the other hand by the total elimination of the OG dye from the solution within about 45 min when using $3CTA^+$–Bd–TiO_2 catalyst instead of 90 min when $5CTA^+$–Bd–TiO_2 sample is involved. This difference in photocatalytic behavior of both TiO_2 supported Bd is due to their different structural, textural and microstructural features as demonstrated above, which are induced by the effect of the surfactant amount used in preparing starting organobeidellite. The coupling of several parameters such as surface area, photocatalyst amount, … could give idea about the efficiency magnitude of a photocatalyst. As the difference between the specific surface area of both the supported photocatalysts investigated herein is not noticeable, their efficiencies and that of pure TiO_2 were compared by normalizing Orange G proportion by mass of titanium converted by photocatalysis in 15 min. Hence, Fig. 11, shows that the supported sample $3CTA^+$–Bd–TiO_2 is almost three times and four times more efficient than TiO_2 alone and $5CTA^+$–Bd–TiO_2, respectively. On the other hand, the most photoactive supported catalyst ($3CTA^+$–Bd–TiO_2) developed herein is more active than the most one based on palygorskite reported elsewhere (Bouna et al., 2011). Nevertheless, it is worth noting that both the clay supported photocatalysts remained largely two times more active than the commercially available TiO_2 Degussa P25.

The different arrangement modes within beidellite interlayer spaces of these species as well as the importance of the adsorption of their excess on external surfaces of clay mineral particles upon

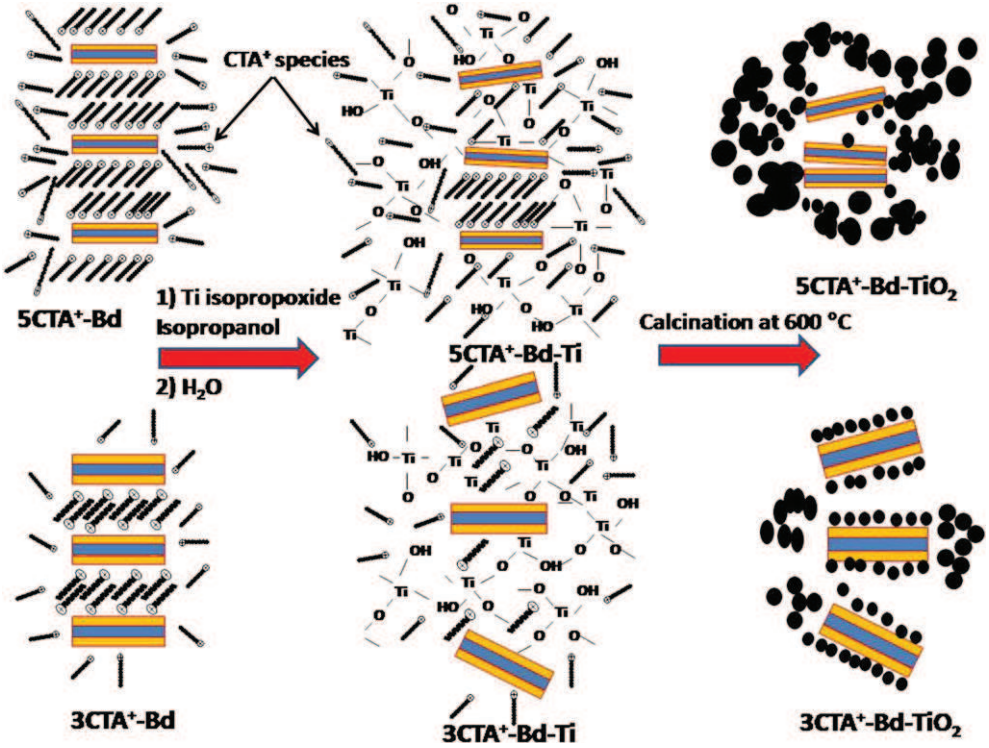

Fig. 12. Adapted schematic illustration from Letaïef et al. (2006) showing the difference in microstructure of TiO_2 developed in different disposition modes of CTA^+ species within organophilic environments created upon organomodification with amounts of CTAB equivalent to 3 and 5 CEC of the beidellite.

modification with an amount equivalent to 3CEC or 5CEC evidenced in part I are likely responsible of the more or the less stabilization of TiO_2 anatase and thus of the difference in catalytic activity of both the derivative supported photocatalysts. Indeed, although the bilayer paraffin disposition of CTA^+ species upon beidellite organomodification with 5CEC probably offers a very organophilic environment favoring the penetration of much Ti precursor (TTIP) between intercalated CTA^+ species as suggested by several authors (Letaïef et al., 2006; Manova et al., 2010; Ruiz-Hitzky and Aranda, 2014), the adsorption of important amount of CTA^+ entities excess on external surfaces of clay mineral particles likely prevents this to be occurred and instead promotes the development of much of TiO_2 assessed by ICP analysis to be around 64.6 wt.% outside Bd interlayer regions. Thus, TiO_2 particles are so close each other that they could undertake sintering upon calcination at 600 °C to allow their size to grow and consequently to exceed critical size required for the transformation of anatase into rutile. Nevertheless, the amount of CTA^+ species adsorbed at external surfaces upon organomodification of beidellite with 3CEC of CTAB is lower in comparison with 5CEC as evidenced by CHN (Table 3 given in the companion paper I: Organobeidellite precursor for nanocomposites) and thermal analyses (Fig. 5) in part I to yield likely Ti alkoxide to get predominantly hydrolyzed and condensed in interlayer spaces formed of monolayer paraffin structure of CTA^+ species. As the amount of CTA^+ intercalated to compensate Bd layers charges is limited and defined by clay mineral CEC, this probably creates an environment less but sufficiently organophilic where the amount of TiO_2 developed was lower around 52.07 as determined by ICP analysis. Accordingly, the contact between TiO_2 particles is relatively reduced so that the occurrence of sintering upon heat treatment is less pronounced. Thereby, this likely yields to developed TiO_2 particles when involving $3CTA^+$–Bd precursor to be kept smaller less than the critical size inducing the stabilization of TiO_2 anatase. Based on results from in-situXRD along with the variation of the average crystallite size, TEM observations and textural characterizations, Fig. 12 schematically summarizes microstructural features of TiO_2 developed starting from $3CTA^+$–Bd or $5CTA^+$–Bd.

4. Conclusion

This study has demonstrated the effect of CTAB surfactant amount, used for preparing organobeidellite starting materials, on physicochemical features and photocatalytic properties of TiO_2 supported Bd nanocomposites in the removal of OG dye from aqueous media. Organomodification of a Bd from Agadir basin (Morocco) with an amount equivalent to 3 CEC of the clay mineral was found to be the optimal amount to produce TiO_2 supported Bd nanocomposites exhibiting advantageous microstructural features in terms of amount of immobilized TiO_2, particle size and distribution, anatase stability and hence improved photocatalytic activity. Besides the valorization of the Bd as a Moroccan natural resource, this study contributed in the optimization of synthesis conditions yielding to efficient TiO_2 supported clay minerals photocatalysts.

Supplementary data to this article can be found online at http://dx.doi.org/10.1016/j.clay.2015.04.025.

Acknowledgments

The financial supports from the “Convention de coopération CNRST-Maroc/CNRS-France” (chemistry project no04/13) and the “Programme d'Action Intégrée Toubkal” (no14/MS/14) are gratefully acknowledged.

References

An, T., Chen, J., Li, G., Ding, X., Sheng, G., Fu, J., Mai, B., 2008. Characterization and photocatalytic activity of TiO_2 immobilized hydrophobic montmorillonite photocatalysts: degradation of decabromodiphenyl ether (BDE 209). Catal. Today 139, 69–76.

Aranda, P., Kun, R., Martin-Luengo, M.A., Letaïef, S., Dékány, I., Ruiz-Hitzky, E., 2008. Titania–sepiolite nanocomposites prepared by a surfactant templating colloidal route. Chem. Mater. 20, 84–91.

Bezrodna, T., Puchkovska, G., Shimanovska, V., 2003. Pyridine–TiO_2 surface interaction as a probe for surface active centers analysis. Appl. Surf. Sci. 214, 222–231.
Bouna, L., Rhouta, B., Amjoud, M., Jada, A., Maury, F., Daoudi, L., Senocq, F., 2010. Correlation between eletrokinetic mobility and ionic dyes adsorption of Moroccan Stevensite. Appl. Clay Sci. 48, 527–530.
Bouna, L., Rhouta, B., Amjoud, M., Maury, F., Lafont, M.-C., Jada, A., Senocq, F., Daoudi, L., 2011. Synthesis, characterization and photocatalytic activity of TiO_2 supported natural palygorskite microfibers. Appl. Clay Sci. 52, 301–311.
Bouna, L., Rhouta, B., Daoudi, L., Maury, F., Amjoud, M., Senocq, F., Lafont, M.C., Jada, A., 2012. Mineralogical and physic-chemical characterisations of ferruginous **Bd** rich clay from Agadir basin (Morocco). Clay Clay Miner. 60, 278–290.
Bouna, L., Rhouta, B., Maury, F., 2013. Physicochemical study of photocatalytic activity of TiO_2 supported palygorskite clay mineral. Int. J. Photoenergy http://dx.doi.org/10.1155/2013/815473 (Article ID 815473, 6 pages).
Bouna, L., Rhouta, B., Maury, F., Jada, A., Senocq, F., Lafont, M.-C., 2014. Photocatalytic activity of TiO2/stevensite nanocomposites for the removal of Orange G from aqueous solutions. Clay Miner. 49, 365–376.
Carp, O., Huisman, C.L., Reller, A., 2004. Photoinduced reactivity of titanium dioxide. Prog. Solid State Chem. 32, 33–177.
Chen, D., Zhu, Q., Zhou, F., Deng, X., Li, F., 2012. Synthesis and photocatalytic performances of the TiO_2 pillared montmorillonite. J. Hazard. Mater. 235–236, 186–193.
Fujishima, A., Zhang, X., 2006. Titanium dioxide photocatalysis: present situation and future approaches. C. R. Chim. 9, 750–760.
Fujishima, A., Rao, T.-N., Tryk, D.-A., 2000. Titanium dioxide photocatalysis. J. Photochem. Photobiol. C 1, 1–21.
Herrmann, J.-M., 1999. Heterogeneous photocatalysis: fundamentals and applications to the removal of various types of aqueous pollutants. Catal. Today 53, 115–129.
Hofstadler, K., Rupert, B., Novalic, S., Heisler, G., 1994. New reactor design for photocatalytic wastewater treatment with TiO_2 immobilized on fused-silica glass fibers: photomineralization of 4-chlorophenol. Environ. Sci. Technol. 28, 670–674.
Houari, M., Saidi, M., Tabet, D., Pichat, P., Khalaf, H., 2005. The removal of 4-chlorophenol and dichloroacetic acid in water using Ti-, Zr- and Ti/Zr-pillared bentonites as photocatalyst. Am. J. Appl. Sci. 2, 1136–1140.
Jada, A., Debih, H., Khodja, M., 2006. Montmorillonite surface properties modifications by asphaltenes adsorption. J. Pet. Sci. Eng. 52, 305–316.
Letaïef, S., Angeles Martin-Luengo, M., Aranda, P., Ruiz-Hitzky, E., 2006. A colloidal route for delamination of layered solids: novel porous-clay nanocomposites. Adv. Funct. Mater. 16, 401–409.
Liu, J., Dong, M., Zuo, S., Yu, Y., 2009. Solvothermal preparation of TiO_2/montmorillonite and photocatalytic activity. Appl. Clay Sci. 43, 156–159.
Manova, E., Aranda, P., Martín-Luengo, M.A., Letaïef, S., Ruiz-Hitzky, E., 2010. New titania-clay nanostructured porous materials. Microporous Mesoporous Mater. 131, 252–260.
Nieto-Suárez, M., Palmisano, G., Ferrer, M.L., Concepción Gutiérrez, M., Yurdakal, S., Augugliaro, V., Pagliaro, M., del Monte, F., 2009. Self-assembled titania–silica–sepiolite based nanocomposites for water decontamination. J. Mater. Chem. 19, 2070–2075.
Paz, Y., 2006. Preferential photodegradation—why and how? C. R. Chim. 9, 774–787.
Rhouta, B., Kaddami, H., Elbarqy, J., Amjoud, M'B., Daoudi, L., Maury, F., Senocq, F., Maazouz, A., Gerard, J.-F., 2008. Elucidation of the structure of the jbel rhassoul stevensite (morocco) by advanced physico-chemical study. Clay Miner. 43, 393–404.
Robertson, P.K.-J., 1996. Semiconductor photocatalysis: an environmentally acceptable alternative production technique and effluent treatment process. J. Cleaner Prod. 4, 203–212.
Ruiz-Hitzky, E., Aranda, P., 2014. Novel architectures in porous materials based on clays. J. Sol-Gel Sci. Technol. 70, 307–316.
Sarantopoulos, C., Gleizes, A.N., Maury, F., Puzenat, E., Guillard, C., Herrmann, J.-M., 2009. Microfibrous TiO_2 supported photocatalysts prepared by metal–organic chemical vapor infiltration for indoor air and waste water purification. Appl. Catal. B Environ. 91, 225–233.
Tong, T., Zhang, J., Tian, B., Chen, F., He, D., 2008. Preparation and characterization of anatase TiO_2 microspheres with porous frameworks via controlled hydrolysis of titanium alkoxide followed by hydrothermal treatment. Mater. Lett. 62, 2970–2972.